The SIRTF First-Look Survey. I. VLA Image and Source Catalog

J. J. Condon, W. D. Cotton, and Q. F. Yin

National Radio Astronomy Observatory[1]*, 520 Edgemont Road, Charlottesville, VA 22903*

jcondon@nrao.edu, bcotton@nrao.edu, qyin@nrao.edu

G. Helou, D. L. Shupe, B. T. Soifer, and L. J. Storrie-Lombardi

SIRTF Science Center, California Institute of Technology, Mail Code 314-6, 1200 East California Boulevard, Pasadena, CA 91125

gxh@ipac.caltech.edu, shupe@ipac.caltech.edu, bts@mop.caltech.edu, lisa@ipac.caltech.edu

and

M. W. Werner

Jet Propulsion Laboratory, California Institute of Technology, 4800 Oak Grove Drive, Pasadena, CA 91109

mww@ipac.caltech.edu

ABSTRACT

The First-Look Survey (FLS) of the Space InfraRed Telescope Facility (SIRTF) will cover about 5 deg^2 centered on J2000 $\alpha = 17^{\rm h}\,18^{\rm m}$, $\delta = +59^\circ\,30'$ in order to characterize the extragalactic infrared sky two orders-of-magnitude deeper than the IRAS survey. We expect that most of the FLS far-infrared ($\lambda = 160$, 70, and $24\,\mu$m) sources will be star-forming galaxies obeying the very tight far-infrared/radio correlation and will be continuum radio sources with flux densities $S \gtrsim 100\,\mu$Jy at $\nu = 1.4$ GHz. Conversely, radio sources stronger than $100\,\mu$Jy are usually powered by star-forming galaxies, plus some active galactic nuclei, and most should be detectable by the SIRTF FLS. Thus a sensitive radio survey can be used to select and identify most of the SIRTF FLS source population before launch. We used the B configuration of the VLA to image the FLS

[1]The National Radio Astronomy Observatory is operated by Associated Universities, Inc., under cooperative agreement with the National Science Foundation.

area at $\nu = 1.4$ GHz with $\sigma_{\rm n} \approx 23\,\mu$Jy beam^{-1} noise, $\theta = 5''$ resolution, and $\sigma_{\alpha,\delta} \lesssim 0\farcs5$ position uncertainties. The resulting radio image and catalog of 3565 radio components brighter than $S_{\rm p} = 5\sigma_{\rm n} = 115\,\mu$Jy beam^{-1} have been released via the web to expedite follow-up optical identification and spectroscopy.

Subject headings: catalogs—galaxies: active—galaxies: starburst—infrared radiation—radio continuum—surveys

1. Introduction

The Space InfraRed Telescope Facility (SIRTF) is the fourth and final element in NASA's family of "Great Observatories." Its 0.85 m telescope and three cryogenically cooled science instruments are capable of performing imaging and spectroscopy in the 3–180 μm wavelength range. Incorporating the latest in large-format infrared detector arrays, SIRTF offers orders-of-magnitude improvements in capability over earlier programs. While SIRTF's mission lifetime requirement remains 2.5 years, recent programmatic and engineering developments have brought a 5-year cryogenic mission within reach. It is currently scheduled for launch into solar orbit in 2003 April.

Following the loss of the Widefield Infrared Explorer (WIRE) mission, a special advisory committee chaired by former STScI Director Bob Williams recommended that SIRTF conduct a First-Look Survey (FLS) using about 100 hours of telescope time to characterize the infrared sky two orders of magnitude deeper than IRAS reached. The FLS (see `http://sirtf.caltech.edu/SSC/fls/`) is essential for effective use of SIRTF mission time because so little is known about faint infrared sources and the cirrus foreground at these levels. A community workshop was convened by B. T. Soifer, director of the SIRTF Science Center (SSC), at Caltech on 1999 September 15 and 16 to define the FLS. The resulting extragalactic FLS should:

(1) detect enough extragalactic sources at unexplored sensitivity levels to generate a representative sample and reduce the uncertainties in the source counts,

(2) characterize the dominant source populations with both the MIPS ($\lambda = 160$, 70, and 24 μm) and IRAC ($\lambda = 8.0$, 5.8, 4.5, and 3.6 μm) detectors from SIRTF plus ancillary optical, near-infrared, and radio surveys, and

(3) explore the moderately high-$|b|$ cirrus foreground and its effect on point-source detectability,

all in time to support the first SIRTF science proposals. The planned FLS consists of a "shallow" survey covering 5 deg^2 and a 3$\times$ deeper "verification" survey of 0.25 deg^2 inside the shallow survey area. The shallow survey is expected to have 5σ detection limits of 27, 4.5, and 1.3 mJy and detect about 400, 1500, and 2500 sources at $\lambda = 160$, 70, and 24 μm, respectively. The corresponding IRAC sensitivity limits will be 60 μJy at $\lambda = 8.0\,\mu$m and 40 μJy at shorter wavelengths. The Infrared Space Observatory (ISO) FIRBACK survey (Puget et al. 1999) at $\lambda = 175\,\mu$m suggests that the FLS will be dominated by a large and strongly evolving population of starburst galaxies at cosmological redshifts, supplemented by a smaller but significant number of AGNs.

Optical and radio surveys are an essential part of the FLS. The principal requirement is for optical identifications, the first step toward understanding FLS sources. If local IRAS sources with the highest FIR/optical flux ratios (Arp 220 for example) were moved to cosmological distances where they would be just above the FLS sensitivity detection limit, they would still be brighter than $R \approx 25.5$ mag. Optical images of this depth were obtained with the CCD Mosaic camera on the NOAO 4 m telescope in 2000 May. Accurate ($\sigma_{\alpha,\delta} < 1''$) positions are needed to make complete and reliable associations of infrared or radio sources with such faint galaxies. However, most of the detected MIPS sources will have flux densities near the 5σ detection limit, so their rms positional uncertainties will be about 10% of the half-intensity beamwidths (Condon 1997), $\sigma_{\alpha,\delta} \approx 2''$ at $\lambda = 70\,\mu$m and $\sigma_{\alpha,\delta} \approx 5''$ at $\lambda = 160\,\mu$m.

A deep radio image covering the FLS area is needed for two reasons: (1) Nearly all far-infrared (FIR) sources obey the tight FIR/radio flux correlation (Condon, Anderson, & Helou 1991) and most radio sources fainter than 1 mJy at 1.4 GHz also appear to be starburst galaxies obeying the FIR/radio correlation (Condon 1989). Thus we expect that the deep FIR and radio source populations are nearly identical. Only radio observations can provide pre-launch images and catalogs that both select most of the several thousand galaxies which will appear in the FIR images and reject the millions of galaxies brighter than $R \approx 25.5$ which will not. (2) The radio image can have the higher resolution and positional accuracy required for making reliable optical identifications on the basis of position coincidence alone. The radio data can be used to select and identify those optical galaxies most likely to be FLS sources for further study before launch. Later, the FIR/radio flux ratios can also be used to distinguish dust-shrouded radio-loud AGN from dusty starburst galaxies.

Only the VLA B-configuration operating at $\nu \approx 1.4$ GHz can efficiently produce radio images with the required sky coverage, sensitivity, and resolution. The effective field-of-view $\Omega_\mathrm{e} \approx \pi\theta_\mathrm{p}^2/(8\ln 2)$ for surveys is only half the primary-beam solid angle (Condon et al. 1998); $\Omega_\mathrm{e} \approx 1/7$ deg^2 for the $\theta_\mathrm{p} \approx 31'$ primary beamwidth of the VLA at 1.4 GHz. Thus 35 partially overlapping fields are required to make a mosaic image covering the 5 deg^2 FLS area with nearly uniform sensitivity. The 1.4 GHz detection limits needed to match the MIPS shallow survey are $5\sigma_{\rm n} \lesssim 100\,\mu$Jy. This estimate is based on the following assumptions: (1) $\langle S(60\,\mu{\rm m})/S(1.4\,{\rm GHz})\rangle \approx 140$ in the source frame, (2) most radio sources have spectral indices $\alpha \approx 0.7$, (3) most FIR sources have the average spectra of sources in the IRAS Bright Galaxy Sample (Soifer et al. 1989), and (4) the median redshift of the fainter FLS sources is $\langle z \rangle \lesssim 1$. The VLA can approach this sensitivity after about 7 hours of integration per field. The B-configuration resolution is $5''$ FWHM (full width between half-maximum points), so the rms confusion $\sigma_{\rm c} \approx 1$ μJy beam^{-1} is negligible and even the faintest detectable ($5\sigma_{\rm n}$) sources will have $\sigma_{\alpha,\delta} \approx 0\farcs5$ position uncertainties.

The scientific value of the optical and radio surveys is greatest if they can be completed before launch. To ensure that the FLS area will be visible to SIRTF immediately after the in-orbit checkout, the FLS must be located inside the Constant Viewing Zone (CVZ) within 10° of an ecliptic pole . In the northern CVZ the region having the lowest cirrus brightness (1–2 MJy sr^{-1} at $\lambda = 100\,\mu$m) lies near J2000 $\alpha = 17^{\rm h}\ 00^{\rm m}$, $\delta = +61^\circ$ (Schlegel, Finkbeiner, & Davis 1998). The FLS center position $\alpha = 17^{\rm h}\ 18^{\rm m}$, $\delta = +59^\circ\ 30'$ is offset slightly to avoid relatively strong ($S > 300$ mJy) radio sources whose sidelobes can degrade VLA images.

Like the NVSS (Condon et al. 1998), the VLA portion of the FLS was made as a service to the astronomical community. The principal data products are available at the NRAO web site `http://www.cv.nrao.edu/sirtf_fls/` and at also at the SIRTF web site `http://sirtf.caltech.edu/`. They include FITS-format images, source catalogs, and user software for browsing the catalog and extracting postage-stamp subimages.

2. VLA Observations and Data Analysis

The area covered by the FLS is much larger than the VLA primary beam at $\nu = 1.4$ GHz, a Bessel function $\theta_{\rm P} = 30\farcm83$ between half-power points, so we covered it by pointing at 35 positions selected from the NVSS pointing grid. The pointing centers and the boundary of the region covered by the final VLA image are shown in Figure 1.

The observations were made during two successive B-configuration sessions of the VLA, 2001 February through May and 2002 June through August. We used the 4-IF mode which provides right and left circular polarizations at both 1.365 GHz and 1.435 GHz. To minimize bandwidth smearing, each IF was divided into seven spectral channels of bandwidth 3.125 MHz. The nearby phase calibrator 1634+627 was observed about four times per hour to track atmospheric phase fluctuations closely, and the intensity calibrator 3C 286 was observed at the beginning of each observing run. The assumed flux densities of 3C 286 were

$S(1.365\,\mathrm{GHz}) = 15.01\,\mathrm{Jy}$ and $S(1.435\,\mathrm{GHz}) = 14.65\,\mathrm{Jy}$.

The calibrated and edited (u, v) data from each pointing were imaged separately with the special AIPS task VLALB. It incorporates many of the automatic imaging features from the NVSS imaging task VLAD (Condon et al. 1998). In addition, it accurately images the curved sky by breaking the main field-of-view, a spherical cap with radius $45'$, into a fly's eye of $\sim 10^2$ smaller fields, each of which is a plane whose center is tangent to the spherical sky. After cleaning and restoration with a $5''$ FWHM circular Gaussian beam, the small fields were flattened onto the final image plane. All but two of the 35 fields were imaged with ROBUST = 0.7 weighting, a compromise (u, v)-plane taper that reduces the sidelobes and increases the resolution of the natural dirty beam but multiplies the image noise by about 1.07. The two fields containing the brightest point sources were imaged with ROBUST = 0.5 for higher dynamic range.

The average integration time on one pointing position was about five hours. The theoretical rms noise of a naturally weighted image at each pointing center is about

$$\sigma_{\mathrm{n}} = \frac{\sqrt{2} k_{\mathrm{B}} T_{\mathrm{s}}}{\eta_{\mathrm{a}} \eta_{\mathrm{c}} A \sqrt{N_{\mathrm{b}} N_{\mathrm{IF}} \tau \Delta\nu}}$$

(Crane & Napier 1989), where $k_{\mathrm{B}} \approx 1.38 \times 10^{-23}$ J K^{-1} is the Boltzmann constant, $T_{\mathrm{s}} \approx 40$ K is the system temperature at the typical zenith angle of our observations, $\langle z \rangle \approx 40^\circ$, $\eta_{\mathrm{a}} = 0.51$ is the aperture efficiency, $\eta_{\mathrm{c}} \approx 0.77$ is the correlator efficiency, A is the geometric area of one 25 m telescope, $N_{\mathrm{b}} = 351$ is the number of baselines when all 27 telescopes are in the array, $N_{\mathrm{IF}} = 4$, $\tau \approx 1.8 \times 10^4\,\mathrm{s}$ is the mean integration time per field, and $\Delta\nu \approx 7 \times 3.125\,\mathrm{MHz}$ is the total bandwidth of one IF. The theoretical noise is $\sigma_{\mathrm{n}} \approx 19\,\mu\mathrm{Jy\ beam}^{-1}$ for our choice of (u, v) weighting. In practice, not all telescopes were available continuously and some images are limited by dyamic range. We measured $\sigma_{\mathrm{n}} \approx 21.5\,\mu\mathrm{Jy\ beam}^{-1}$ at the centers of most images and slightly higher values in images containing the strongest sources.

The final image is a weighted sum of the $m = 35$ individual images. The weight W_i assigned to the brightness b_i of any pixel from an individual image is equal to the square of the normalized primary power pattern at that pixel; this weight is proportional to the square of the expected sensitivity. Calculating the final image brightnesses from

$$B = \sum_{i=1}^{m} W_i b_i / \sum_{i=1}^{m} W_i$$

simultaneously maximizes the overall sensitivity and corrects for primary-beam attenuation. The pixel weights in the final image are

$$W = \sum_{i=1}^{m} W_i \ ,$$

and the local noise level should be proportional to $W^{-1/2}$. A pixel with $W = 1.00$ has the same theoretical sensitivity as the center of one individual image, and we blanked all pixels having $W < 0.64$ to truncate the edges of the weighted image. The distribution of pixel weights in the final blanked image is shown in Fig. 2. The mean weight is $\langle W \rangle \approx 0.879$, so the rms noise averaged over the entire final image should be about $21.5\,\mu$Jy $\times \langle W \rangle^{-1/2} \approx 23\,\mu$Jy. The actual distribution of pixel brightnesses in the final image is shown as a logarithmic histogram in Figure 3. It is consistent with the superposition of a Gaussian noise distribution with rms amplitude $\sigma_{\rm n} = 23.0\,\mu$Jy beam^{-1}, a weak negative-going tail caused by uncleaned sidelobes of strong sources, and a long positive-going tail representing genuine radio sources.

3. Results

A small portion of the final radio image is displayed in Figure 4. Most of the fainter sources are unresolved or only slightly resolved by the $5''$ FWHM Gaussian restoring beam, but there are a few examples of extended double, triple, or more complex morphologies among the brighter sources, the triple source centered on $\alpha = 17^{\rm h}\,17^{\rm m}\,33\overset{\rm s}{.}8$, $\delta = +67^\circ\,07'\,47''$ for example. Such a distribution of angular sizes and morphologies is expected in samples complete to $S \sim 115\,\mu$Jy (Condon 1989). Most sources slightly stronger than $S \sim 1$ mJy have 1.4 GHz spectral luminosities $L \sim 10^{24}$ W Hz^{-1} and are powered by low-luminosity active galactic nuclei. Their median angular size is greater than $5''$, so many are well resolved. In contrast, significantly weaker sources are more likely to be powered by and coextensive with star formation in distant galaxies whose angular sizes are less than $5''$.

Since most of the faint sources are not significantly resolved, most of the information in the image is well represented by a catalog of elliptical Gaussian components. The free parameters of each fitted Gaussian are peak brightness, right ascension, declination, FWHM major and minor diameters, and major-axis position angle. However, freely fitted diameters smaller than the restoring beamwidth are formally impossible. When they were found, they were fixed at $5''$ and the fit was repeated. From the fitted parameters we calculated the integrated flux density and deconvolved angular diameters (or upper limits). Uncertainties in these parameters were estimated from the same error-propagation model for two-dimensional Gaussian fits used for the NVSS (Condon 1997; Condon et al. 1998) with assumed calibration uncertainties of $0\overset{''}{.}1$ in each coordinate and 3% in flux density. The final component catalog contains nearly all components brighter than $S_{\rm p} = 115\,\mu$Jy beam$^{-1} \approx 5\sigma$; a few that appear to be sidelobes near strong sources were rejected. Most of the surviving components are astronomically distinct radio sources, but 105 groups of two or more components are probably extended radio sources. We labeled the components comprising these groups by their group numbers G001 through G105. Table 1 lists all 3565 radio components in right-ascension order, and the individual columns specify:

Column (1).—Right ascension (J2000) and its rms uncertainty.

Column (2).—Declination (J2000) and its rms uncertainty.

Column (3).—Integrated flux density (mJy) and its rms uncertainty.

Column (4).—Deconvolved FWHM major axis (arcsec) and its rms uncertainty, else a 98% confidence upper limit.

Column (5).—Deconvolved FWHM minor axis (arcsec) and its rms uncertainty, else a 98% confidence upper limit.

Column (6).—Major-axis position angle (degrees east of north) and its rms uncertainty.

Column (7).—X-pixel location in the final image.

Column (8).—Y-pixel location in the final image.

Column (9).—Group number for groups of components that appear to comprise complex radio sources.

To avoid ambiguity, please refer to radio components in the FLS VLA catalog by their full IAU designations (Lortet et al. 1994) of the form FLSVLA JHHMMSS.s+DDMMSS, where FLSVLA is the catalog acronym, J specifies the coordinate equinox J2000.0, HHMMSS.s concatenates the hours, minutes, seconds, and truncated (not rounded) decimal seconds of right ascension, and +DDMMSS represents the degrees, arcminutes, and truncated (not rounded) arcseconds of declination. Thus the radio component at J2000 $\alpha = 17^{\rm h}\,07^{\rm m}\,50\overset{\rm s}{.}959$, $\delta = +59^\circ\,40'\,27\overset{''}{.}99$ should be called FLSVLA J170750.9+594027.

Our estimates for the positions and flux densities of the 105 multicomponent sources are given in Table 2. Normally the positions listed are either the centroids of simple double sources or the fitted positions of central components in triples, and the flux densities are the sums of the group component flux densities. Using radio morphology alone to combine groups of components into astrophysically distinct sources is only educated guesswork, so these "sources" should be regarded as tentative and their resulting parameters as uncertain. Those complex sources whose brightness distributions are not well approximated by two elliptical Gaussians are plotted in Figures 5–13.

The radio image, component catalog, and user software for extracting postage-stamp subimages and browsing the catalog are available via the web at `http://www.cv.nrao.edu/sirtf_fls/` and `http://sirtf.caltech.edu/`.

Q. F. Yin was supported in part by Jet Propulsion Laboratory contract number 1234549.

REFERENCES

Condon, J. J. 1989, ApJ, 338, 13

Condon, J. J. 1997, PASP, 109, 166

Condon, J. J., Anderson, M. A., & Helou, G. 1991, ApJ, 376, 95

Condon, J. J., Cotton, W. D., Greisen, E. W., Yin, Q. F., Perley, R. A., Taylor, G. B., & Broderick, J. J. 1998, AJ, 115, 1693 (NVSS)

Crane, P. C., & Napier, P. J. 1989, in ASP Conf. Ser. 6, Synthesis Imaging in Radio Astronomy, ed. R. A. Perley, F. R. Schwab, & A. H. Bridle (San Francisco: ASP), 139

Lortet, M.-C., Borde, S., & Ochsenbein, F. 1994, A&AS, 107, 193

Puget, J. L. et al. 1999, A&A, 345, 29

Schlegel, D. J., Finkbeiner, D. P., & Davis, M. 1998, ApJ, 500, 525

Soifer, B. T., Boehmer, L., Neugebauer, G., & Sanders, D. B. 1989, AJ, 98, 766

Table 1. Component Catalog

Right Ascension (J2000)	Declination (J2000)	Flux density (mJy)	Major axis (arcsec)	Minor axis (arcsec)	PA (deg)	Pixel X	Pixel Y	Group code
17 07 50.959 $\pm$ 0.016	+59 40 27.99 $\pm$ 0.21	0.721 $\pm$ 0.086	4.6 $\pm$ 0.6	3.1 $\pm$ 0.6	−66.5 $\pm$ 13.2	7171.90	4574.45	
17 07 51.518 $\pm$ 0.027	+59 41 25.98 $\pm$ 0.33	0.213 $\pm$ 0.025	$<$ 5.1	$<$ 3.7		7167.61	4612.99	
17 07 51.592 $\pm$ 0.023	+59 41 40.08 $\pm$ 0.34	0.198 $\pm$ 0.023	$<$ 3.8	$<$ 3.8		7166.88	4622.36	
17 07 52.656 $\pm$ 0.018	+59 39 33.74 $\pm$ 0.26	0.269 $\pm$ 0.024	$<$ 3.4	$<$ 3.2		7164.72	4537.97	
17 07 54.370 $\pm$ 0.015	+59 46 40.54 $\pm$ 0.27	0.358 $\pm$ 0.029	$<$ 4.5	$<$ 3.5		7145.26	4822.04	
17 07 56.475 $\pm$ 0.014	+59 46 33.94 $\pm$ 0.20	0.399 $\pm$ 0.028	$<$ 3.9	$<$ 2.7		7134.83	4817.25	
17 07 58.187 $\pm$ 0.043	+59 15 34.73 $\pm$ 0.68	0.142 $\pm$ 0.027	$<$ 7.1	$<$ 6.3		7172.97	3578.01	
17 08 00.440 $\pm$ 0.038	+59 12 48.21 $\pm$ 0.60	0.123 $\pm$ 0.023	$<$ 5.7	$<$ 5.3		7165.62	3466.62	
17 08 01.574 $\pm$ 0.007	+60 10 57.97 $\pm$ 0.10	7.703 $\pm$ 0.328	$<$ 2.0	$<$ 1.6		7072.57	5791.91	
17 08 03.310 $\pm$ 0.048	+60 10 56.95 $\pm$ 1.03	0.162 $\pm$ 0.033	$<$ 11.1	$<$ 7.1		7063.96	5790.91	
17 08 03.647 $\pm$ 0.022	+59 42 24.58 $\pm$ 0.44	0.220 $\pm$ 0.026	$<$ 5.9	$<$ 3.7		7104.95	4649.72	
17 08 06.316 $\pm$ 0.028	+60 04 09.15 $\pm$ 0.98	0.320 $\pm$ 0.079	8.3 $\pm$ 1.9	$<$ 5.2	−2.7 $\pm$ 8.6	7059.13	5518.57	
17 08 07.474 $\pm$ 0.017	+59 44 19.49 $\pm$ 0.26	0.324 $\pm$ 0.027	$<$ 4.6	$<$ 3.0		7082.81	4725.57	
17 08 09.073 $\pm$ 0.029	+60 08 39.01 $\pm$ 0.88	0.166 $\pm$ 0.028	$<$ 9.7	$<$ 4.4		7038.71	5697.90	
17 08 10.051 $\pm$ 0.015	+59 14 17.29 $\pm$ 0.21	0.431 $\pm$ 0.031	$<$ 4.1	$<$ 3.6		7114.25	3524.15	
17 08 10.283 $\pm$ 0.032	+59 37 36.33 $\pm$ 0.61	0.229 $\pm$ 0.032	$<$ 8.3	$<$ 5.8		7078.59	4456.39	
17 08 11.150 $\pm$ 0.049	+59 47 55.37 $\pm$ 0.79	0.189 $\pm$ 0.034	$<$ 9.1	$<$ 8.5		7058.97	4868.74	
17 08 11.487 $\pm$ 0.037	+59 14 59.70 $\pm$ 0.67	0.183 $\pm$ 0.030	$<$ 8.0	$<$ 6.2		7105.86	3552.14	
17 08 11.553 $\pm$ 0.037	+59 24 42.00 $\pm$ 0.56	0.117 $\pm$ 0.022	$<$ 5.1	$<$ 5.1		7091.21	3940.16	
17 08 11.939 $\pm$ 0.036	+60 09 32.08 $\pm$ 0.67	0.129 $\pm$ 0.024	$<$ 6.7	$<$ 4.9		7023.14	5732.74	
17 08 12.891 $\pm$ 0.030	+59 59 05.14 $\pm$ 0.46	0.144 $\pm$ 0.022	$<$ 4.5	$<$ 4.5		7033.79	5314.75	
17 08 13.113 $\pm$ 0.009	+59 49 10.44 $\pm$ 0.13	0.799 $\pm$ 0.040	$<$ 2.6	$<$ 2.0		7047.26	4918.40	
17 08 13.662 $\pm$ 0.044	+59 47 36.64 $\pm$ 0.78	0.175 $\pm$ 0.029	$<$ 10.5	$<$ 4.3		7046.80	4855.79	
17 08 14.502 $\pm$ 0.007	+59 58 57.20 $\pm$ 0.10	3.734 $\pm$ 0.206	3.0 $\pm$ 0.2	2.5 $\pm$ 0.2	−78.0 $\pm$ 7.7	7025.92	5309.17	G001
17 08 14.836 $\pm$ 0.039	+60 11 22.76 $\pm$ 0.48	0.174 $\pm$ 0.027	$<$ 6.7	$<$ 5.2		7006.03	5805.97	
17 08 15.572 $\pm$ 0.007	+59 59 00.66 $\pm$ 0.10	4.450 $\pm$ 0.243	2.7 $\pm$ 0.2	2.7 $\pm$ 0.2	54.2 $\pm$ 90.0	7020.49	5311.27	G001
17 08 16.009 $\pm$ 0.007	+59 30 01.37 $\pm$ 0.10	3.312 $\pm$ 0.142	$<$ 1.9	$<$ 1.7		7060.74	4152.15	

Note. — Table 1 is presented in its entirety in the electronic edition of the *Astronomical Journal*. A portion is shown here for guidance regarding its form and content.

Table 2. Multicomponent Source Catalog

Component Group	Number of Components	Right Ascension (J2000)	Declination (J2000)	Flux density (mJy)	Figure
G001	2	17 08 15.08	+59 58 59.1	8.18	
G002	4	17 08 17.42	+59 46 29.9	44.33	5a
G003	2	17 08 23.79	+59 59 06.3	1.22	
G004	2	17 08 38.64	+59 44 03.9	21.91	5b
G005	2	17 08 43.05	+59 31 40.2	33.81	
G006	2	17 08 46.65	+59 32 23.0	4.51	5c
G007	2	17 09 21.16	+60 01 30.4	3.89	
G008	4	17 09 26.57	+59 39 36.6	34.62	5d
G009	2	17 09 42.49	+60 12 03.2	26.42	5e
G010	4	17 09 53.78	+59 48 38.2	1.61	5f
G011	2	17 09 56.33	+59 57 31.7	3.90	5g
G012	2	17 10 15.99	+59 20 18.5	14.89	5h
G013	2	17 10 33.24	+59 36 04.9	1.61	
G014	2	17 10 44.33	+59 54 56.7	1.35	6a
G015	6	17 11 05.32	+59 57 50.2	3.16	6b
G016	2	17 11 15.99	+59 56 31.7	28.77	
G017	2	17 11 17.85	+60 19 28.0	34.02	6c
G018	3	17 11 18.34	+59 12 12.6	2.23	
G019	2	17 11 31.77	+59 39 17.0	26.33	
G020	7	17 11 45.40	+60 08 08.7	23.64	6d
G021	2	17 11 47.89	+58 40 11.5	12.08	6e
G022	2	17 12 06.54	+58 52 16.2	1.92	
G023	5	17 12 13.86	+59 17 24.1	5.95	7a
G024	2	17 12 17.45	+59 00 51.6	8.59	7b
G025	2	17 12 21.16	+58 33 00.3	59.85	7c
G026	13	17 12 28.47	+59 56 34.3	25.08	7d
G027	2	17 12 37.92	+59 05 06.4	3.32	
G028	2	17 12 39.49	+58 41 45.2	1.49	
G029	2	17 12 45.07	+58 59 47.8	4.80	7e
G030	3	17 12 48.11	+59 14 31.1	12.86	7f
G031	5	17 13 19.41	+59 20 02.8	5.38	7g
G032	2	17 13 40.84	+59 49 19.7	0.86	
G033	3	17 13 43.04	+58 45 36.8	6.53	7h
G034	2	17 13 50.03	+58 27 43.1	2.61	
G035	2	17 14 02.72	+58 46 22.4	19.82	8a
G036	2	17 14 14.14	+59 47 56.0	15.90	8b
G037	5	17 14 30.85	+60 36 06.4	37.51	8c
G038	2	17 14 35.83	+59 47 20.9	11.74	8d
G039	3	17 14 40.33	+60 04 01.3	30.31	8e
G040	2	17 14 46.02	+58 35 19.5	1.22	
G041	2	17 14 47.74	+58 53 50.8	8.26	
G042	2	17 14 52.13	+59 12 36.4	3.73	
G043	5	17 14 57.85	+59 15 39.7	25.02	8f
G044	2	17 15 08.96	+58 45 27.0	10.11	8g
G045	2	17 15 46.93	+59 17 06.0	17.53	
G046	2	17 16 22.70	+59 15 30.8	14.75	
G047	9	17 16 39.36	+59 15 13.4	19.65	8h

Table 2—Continued

Component Group	Number of Components	Right Ascension (J2000)	Declination (J2000)	Flux density (mJy)	Figure
G048	2	17 16 42.95	+60 23 24.4	2.79	
G049	2	17 16 51.66	+58 12 50.3	10.14	9a
G050	3	17 17 03.00	+60 34 38.4	3.61	9b
G051	2	17 17 19.58	+60 18 17.0	17.65	9c
G052	4	17 17 33.80	+60 07 47.0	20.22	9d
G053	2	17 17 44.25	+59 18 18.4	1.03	9e
G054	3	17 18 21.91	+59 46 59.2	0.64	
G055	2	17 18 29.66	+58 09 13.4	9.64	9f
G056	3	17 18 29.48	+60 52 04.0	32.21	9g
G057	5	17 18 31.63	+60 18 28.1	1.10	9h
G058	8	17 18 41.10	+60 36 28.1	41.71	10a
G059	2	17 18 58.92	+58 27 32.5	3.77	
G060	2	17 19 21.12	+59 09 39.4	4.59	
G061	3	17 19 27.24	+59 59 11.3	1.16	
G062	2	17 19 43.86	+58 17 29.5	2.37	
G063	3	17 19 52.37	+60 14 34.7	103.53	
G064	3	17 19 53.26	+58 52 19.6	5.47	10b
G065	2	17 19 56.18	+59 38 36.0	42.81	
G066	3	17 20 04.01	+58 38 28.0	251.95	
G067	5	17 20 10.26	+59 24 15.2	35.24	10c
G068	3	17 20 09.72	+60 08 02.5	8.51	10d
G069	4	17 20 17.18	+58 20 32.2	9.33	10e
G070	3	17 20 28.26	+59 13 41.6	79.65	10f
G071	2	17 20 30.76	+58 23 00.9	16.65	10g
G072	2	17 20 53.71	+60 29 56.9	1.04	
G073	10	17 21 10.96	+60 12 57.6	57.35	11a
G074	2	17 21 12.37	+59 22 16.2	23.74	11b
G075	3	17 21 16.59	+60 04 06.3	3.24	11c
G076	2	17 21 19.20	+59 37 32.6	38.18	11d
G077	3	17 21 27.32	+60 05 59.0	1.63	11e
G078	3	17 21 30.83	+58 25 58.4	2.77	
G079	2	17 21 47.82	+60 15 48.7	0.64	
G080	3	17 21 48.23	+60 25 31.2	64.14	11f
G081	2	17 21 57.73	+59 15 22.6	8.88	11g
G082	3	17 22 00.58	+60 24 04.2	6.73	11h
G083	4	17 22 05.48	+59 06 50.5	5.27	12a
G084	4	17 22 15.28	+60 22 59.3	48.53	12b
G085	2	17 22 16.36	+58 56 56.3	0.79	
G086	2	17 22 19.59	+59 04 35.0	4.98	12c
G087	2	17 22 45.71	+60 00 04.7	84.02	12d
G088	2	17 22 49.55	+60 26 42.0	2.03	
G089	2	17 22 52.58	+60 07 45.5	0.96	
G090	2	17 23 02.90	+60 29 11.9	6.52	12e
G091	3	17 23 31.95	+60 15 27.2	3.11	12f
G092	4	17 23 33.00	+58 50 35.0	1.57	12g
G093	4	17 23 34.73	+60 19 48.2	4.37	12h
G094	4	17 23 36.85	+59 37 16.1	23.19	12i

Table 2—Continued

Component Group	Number of Components	Right Ascension (J2000)	Declination (J2000)	Flux density (mJy)	Figure
G095	5	17 24 07.77	+59 19 05.6	7.02	13a
G096	2	17 24 34.06	+60 11 31.3	60.96	
G097	7	17 24 39.34	+59 20 44.1	6.84	13b
G098	2	17 24 44.45	+58 42 16.5	8.58	
G099	2	17 24 54.63	+59 13 25.0	2.44	
G100	3	17 24 55.39	+60 24 25.1	56.28	13c
G101	2	17 25 51.47	+59 05 40.5	0.98	13d
G102	5	17 26 25.84	+59 27 03.2	2.58	13e
G103	5	17 26 59.48	+59 40 18.0	37.83	13f
G104	2	17 27 00.54	+59 14 16.2	4.06	
G105	3	17 27 40.73	+58 57 52.7	1.36	

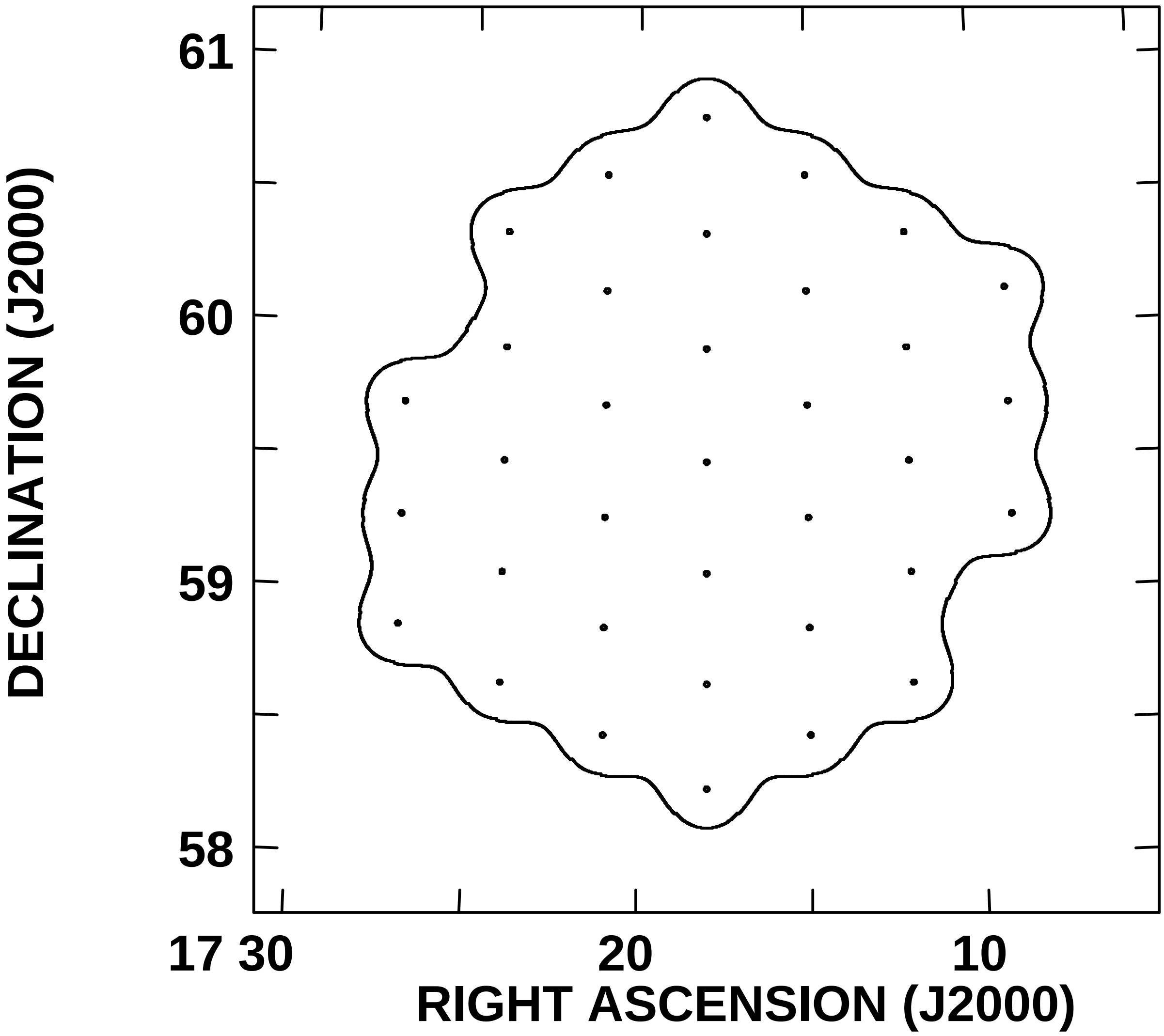

Fig. 1.— The VLA covered the FLS area with a grid of 35 pointings (points). The individual images were mosaiced and the final image was blanked whereever its statistical weight fell below $W = 0.64$ (curved boundary). Abscissa: Right ascension (hours and minutes). Ordinate: Declination (degrees).

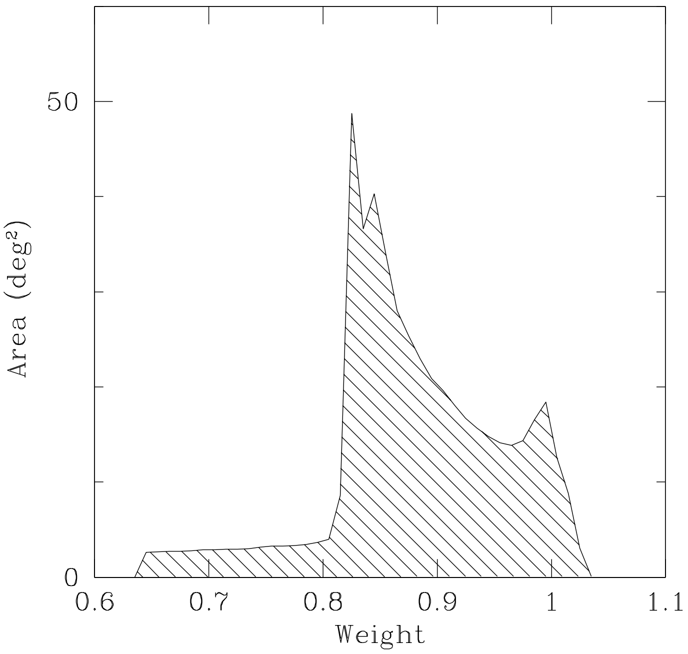

Fig. 2.— The statistical weight distribution of pixels in the VLA image truncated below $W = 0.64$.

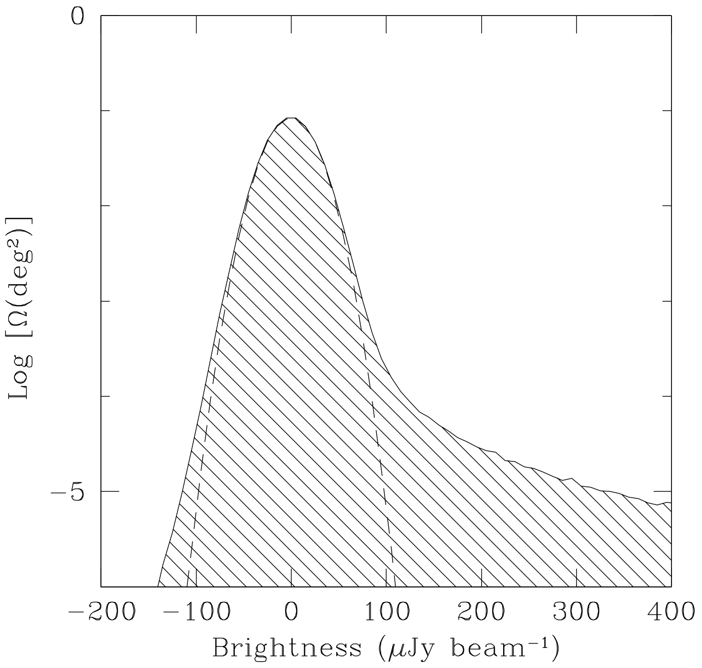

Fig. 3.— The pixel brightness distribution in the VLA image. The broken curve corresponds to Gaussian noise with an rms amplitude $\sigma_{\rm n} = 23\,\mu$Jy beam^{-1}.

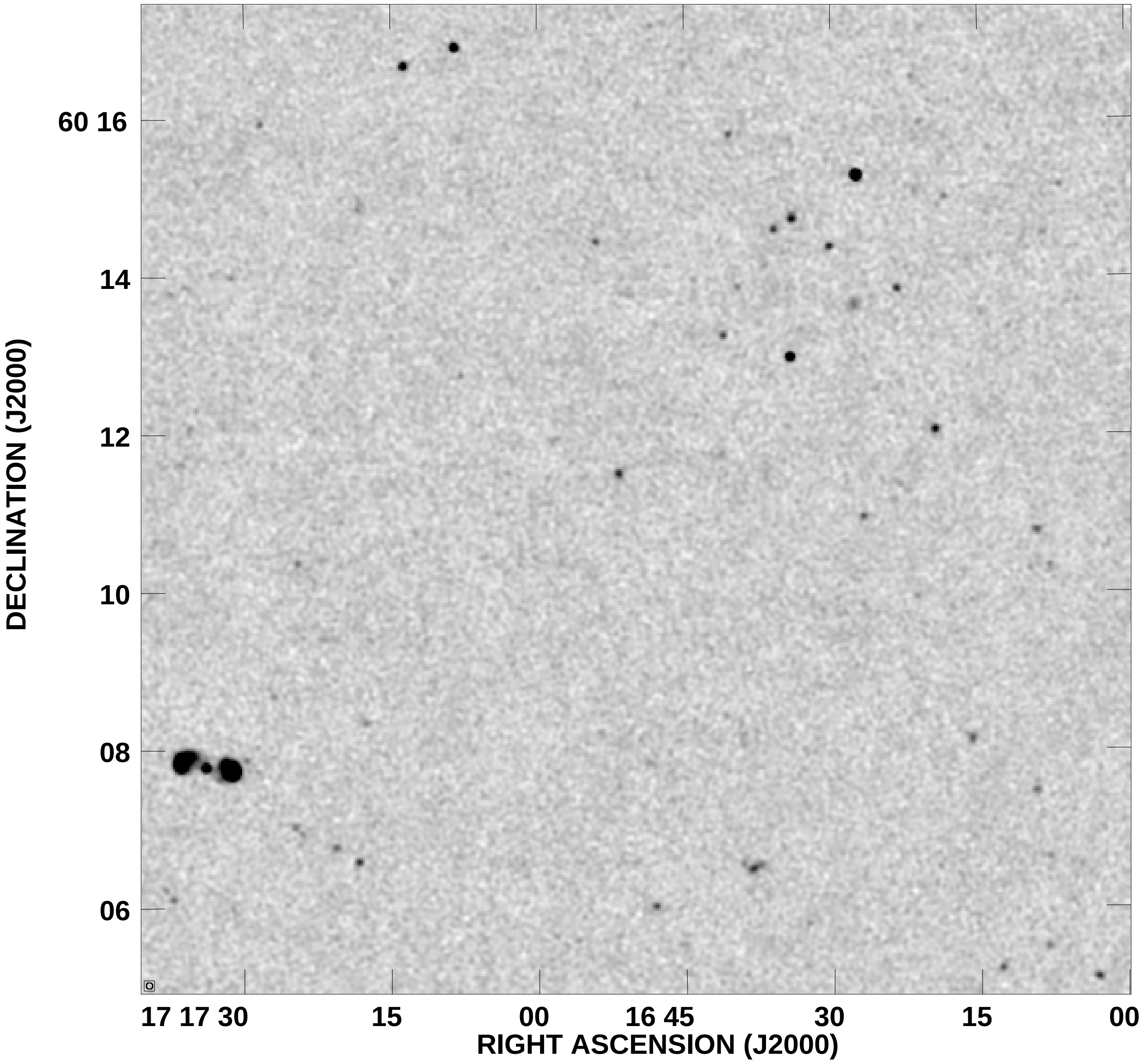

Fig. 4.— This subimage shows ≈ 1% of the FLS area with $\theta = 5''\!.0$ resolution (see the small inset in the lower left corner) and nearly uniform $\sigma_{\rm n} \approx 23\,\mu$Jy noise.

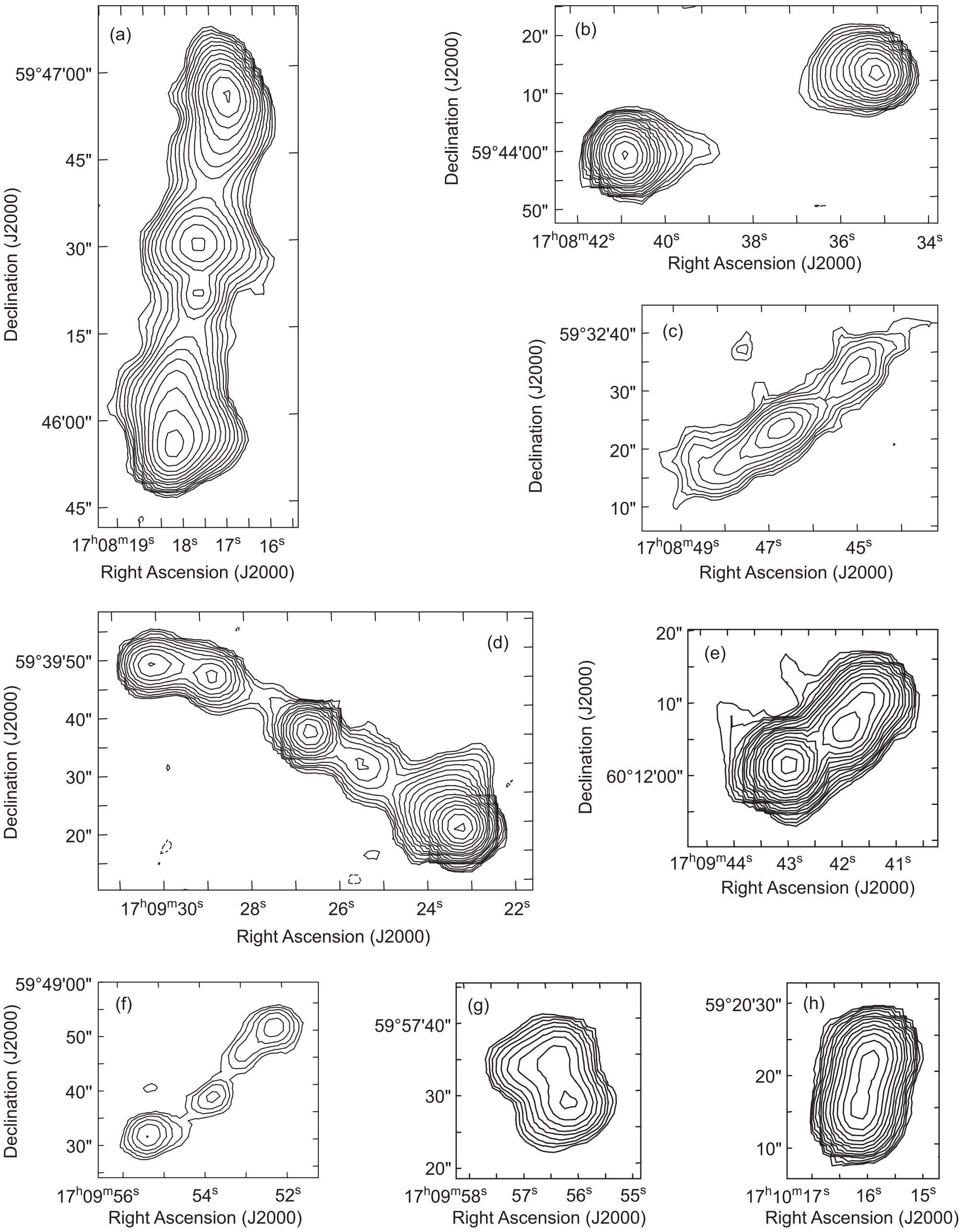

Fig. 5.— Complex sources. Contours are plotted at $\pm 50\,\mu$Jy beam$^{-1} \times 2^{1/2}, 2^{1}, 2^{3/2}, 2^{2}, \ldots$

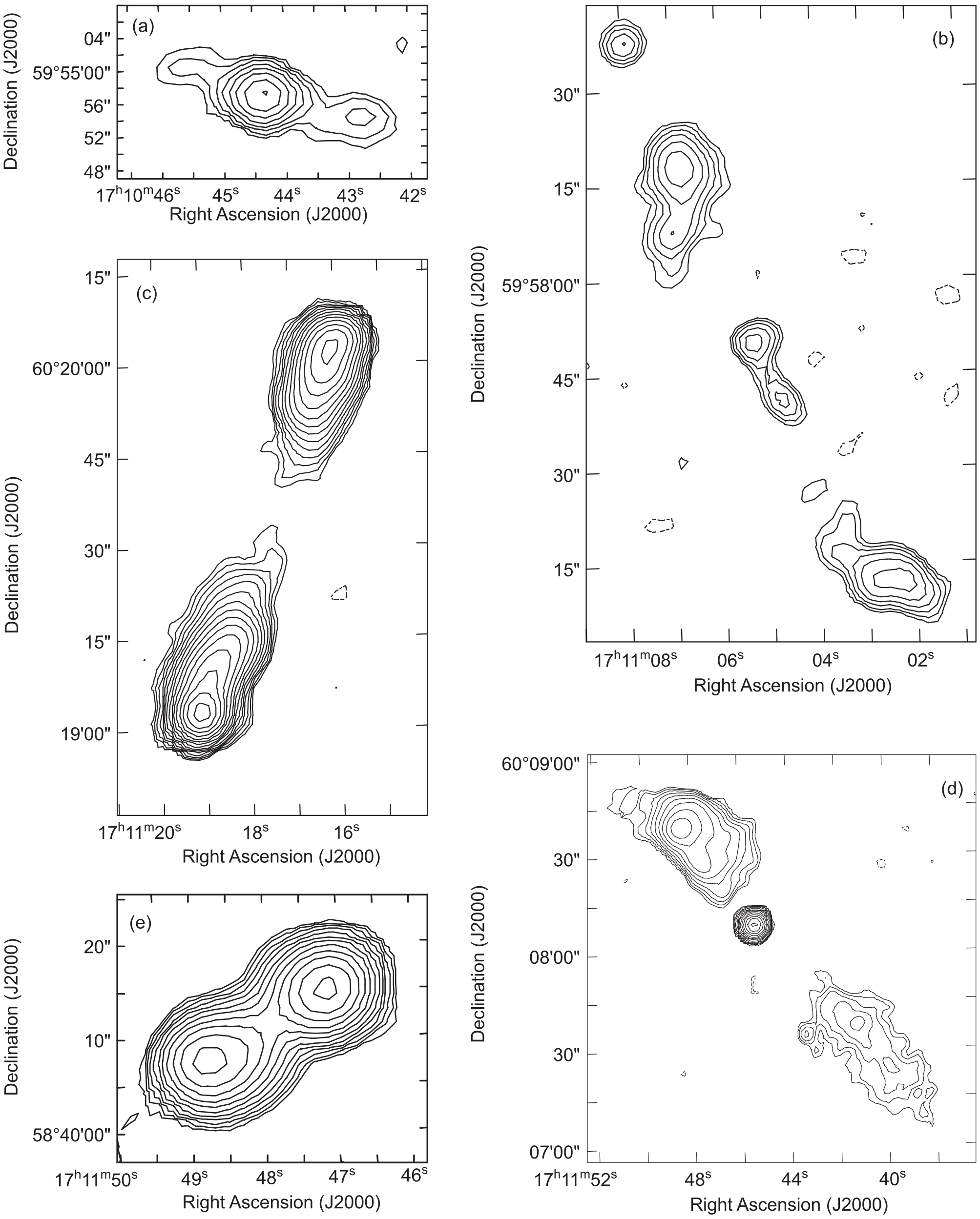

Fig. 6.— Complex sources. Contours are plotted at $\pm 50\,\mu$Jy beam$^{-1}\times 2^{1/2}, 2^{1}, 2^{3/2}, 2^{2}, \ldots$

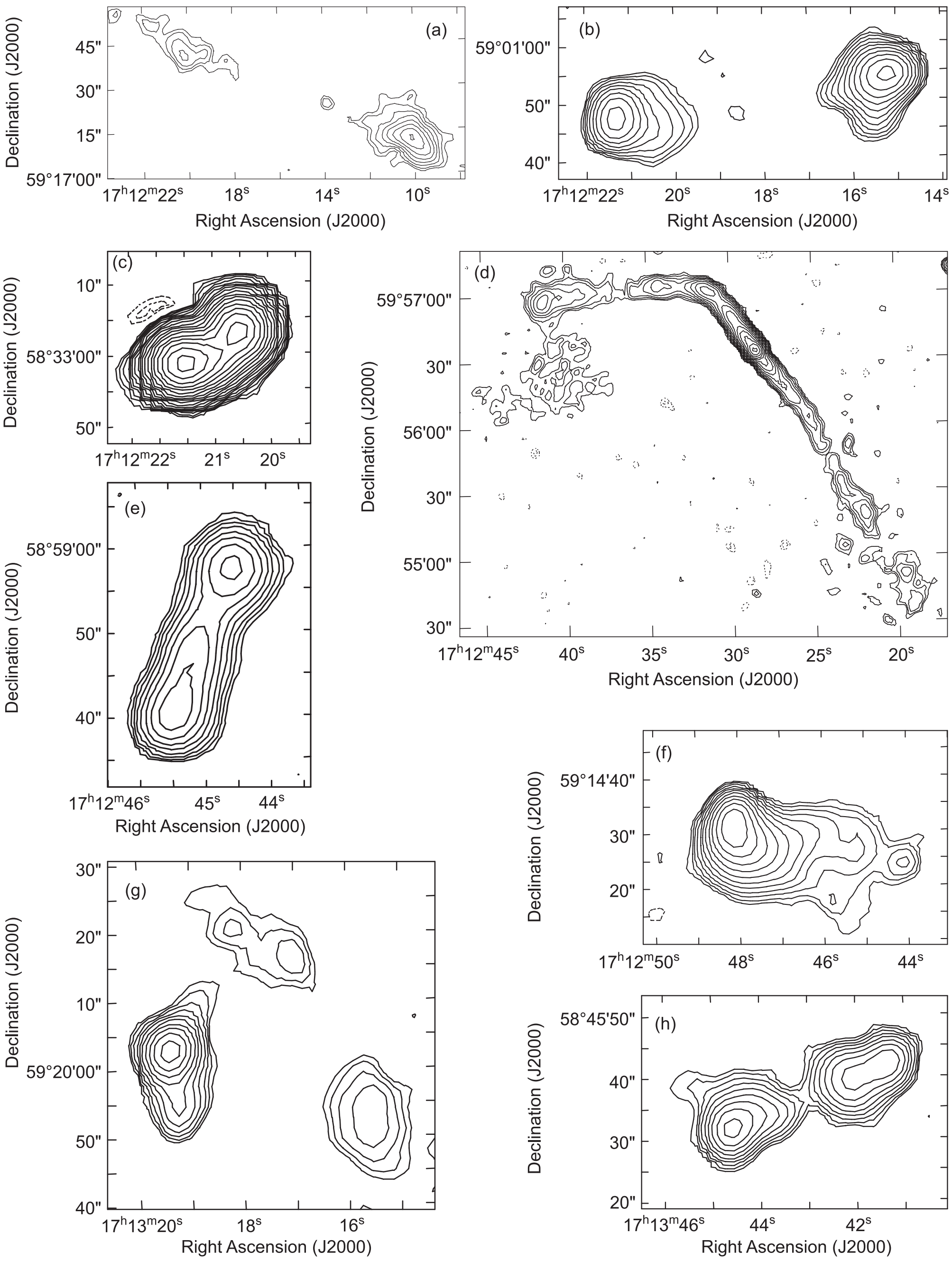

Fig. 7.— Complex sources. Contours are plotted at $\pm 50\,\mu$Jy beam$^{-1} \times 2^{1/2}, 2^{1}, 2^{3/2}, 2^{2}, \ldots$

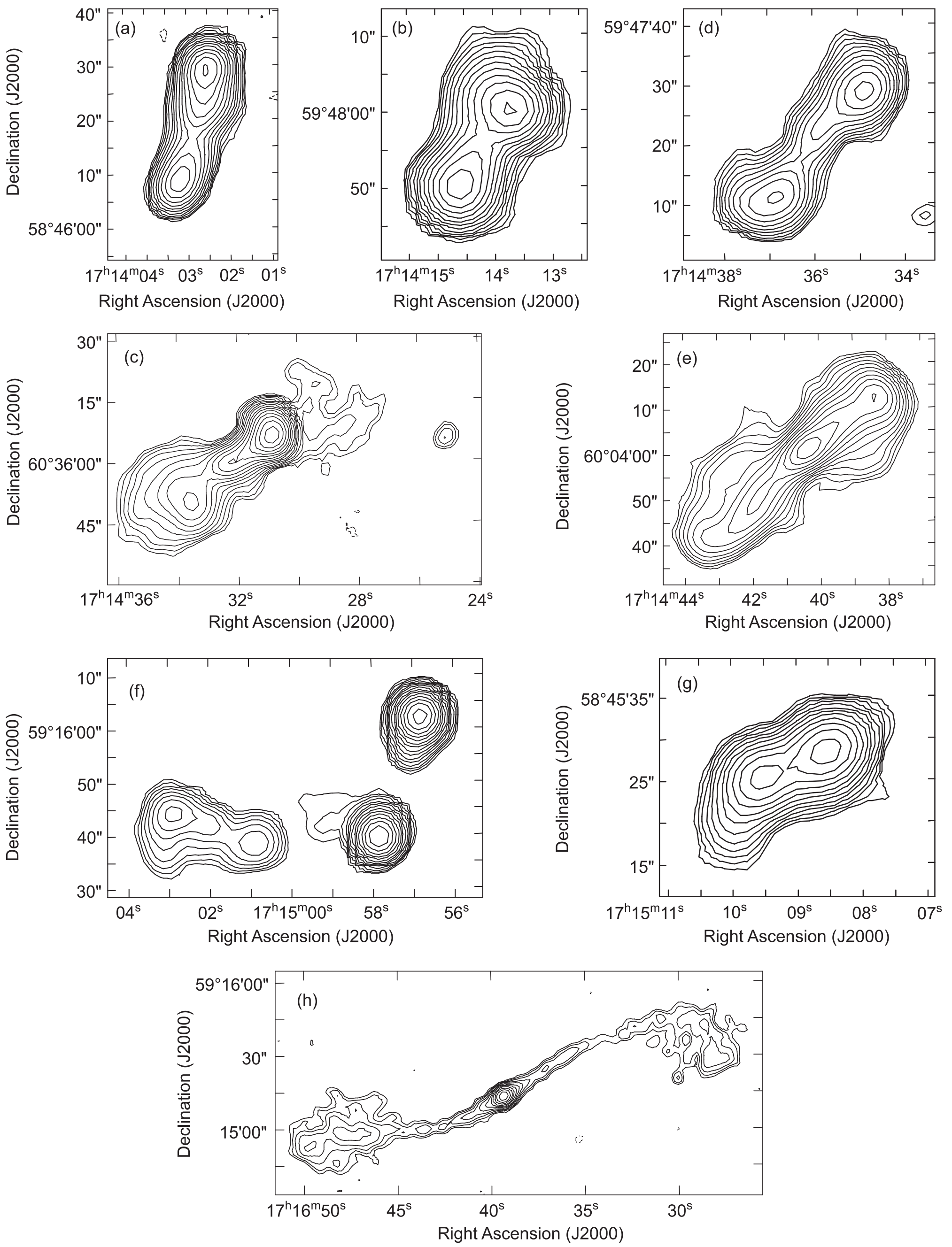

Fig. 8.— Complex sources. Contours are plotted at $\pm 50\,\mu$Jy beam^{-1} $\times\, 2^{1/2}, 2^1, 2^{3/2}, 2^2, \ldots$

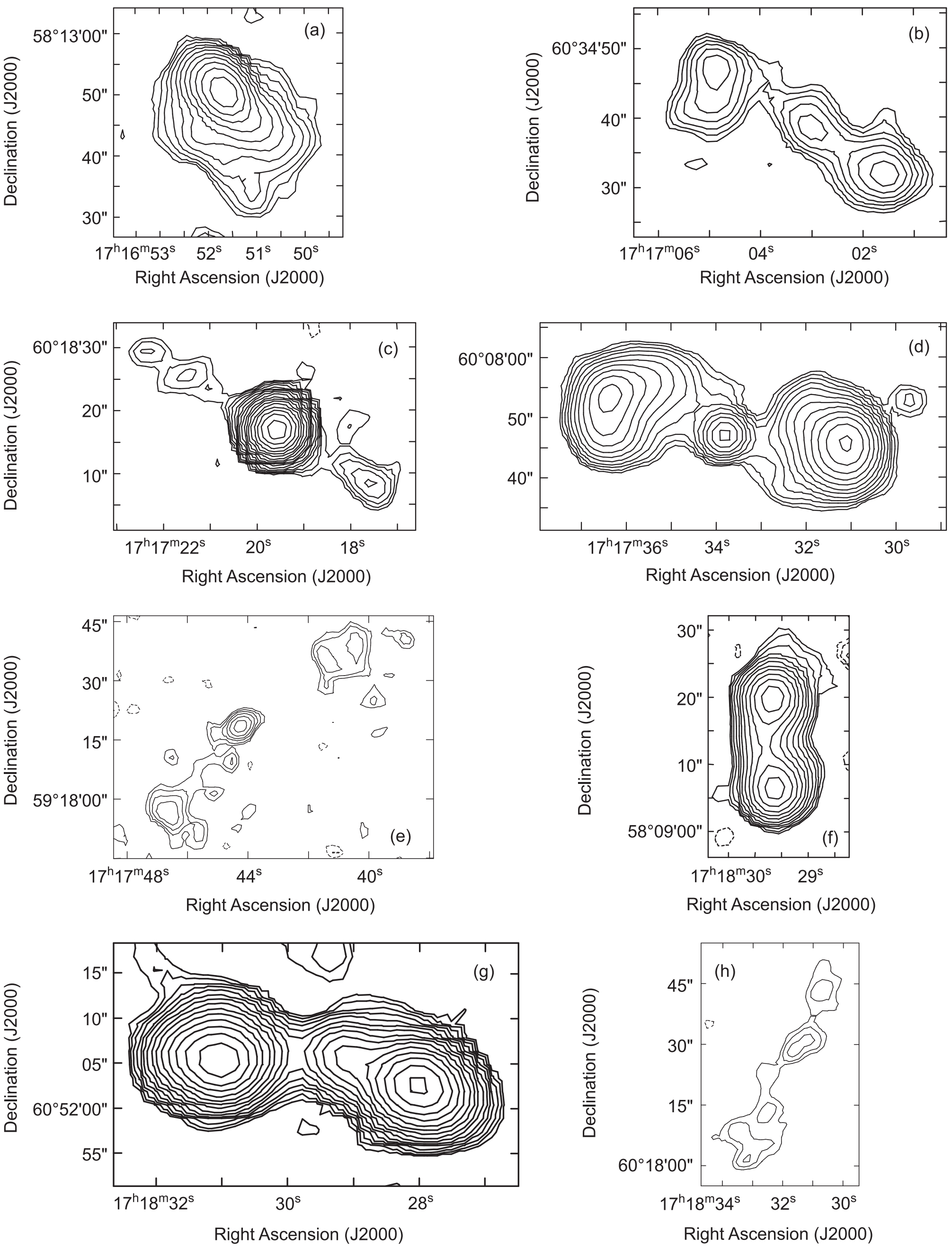

Fig. 9.— Complex sources. Contours are plotted at $\pm 50\,\mu$Jy beam$^{-1} \times 2^{1/2}, 2^{1}, 2^{3/2}, 2^{2}, \ldots$

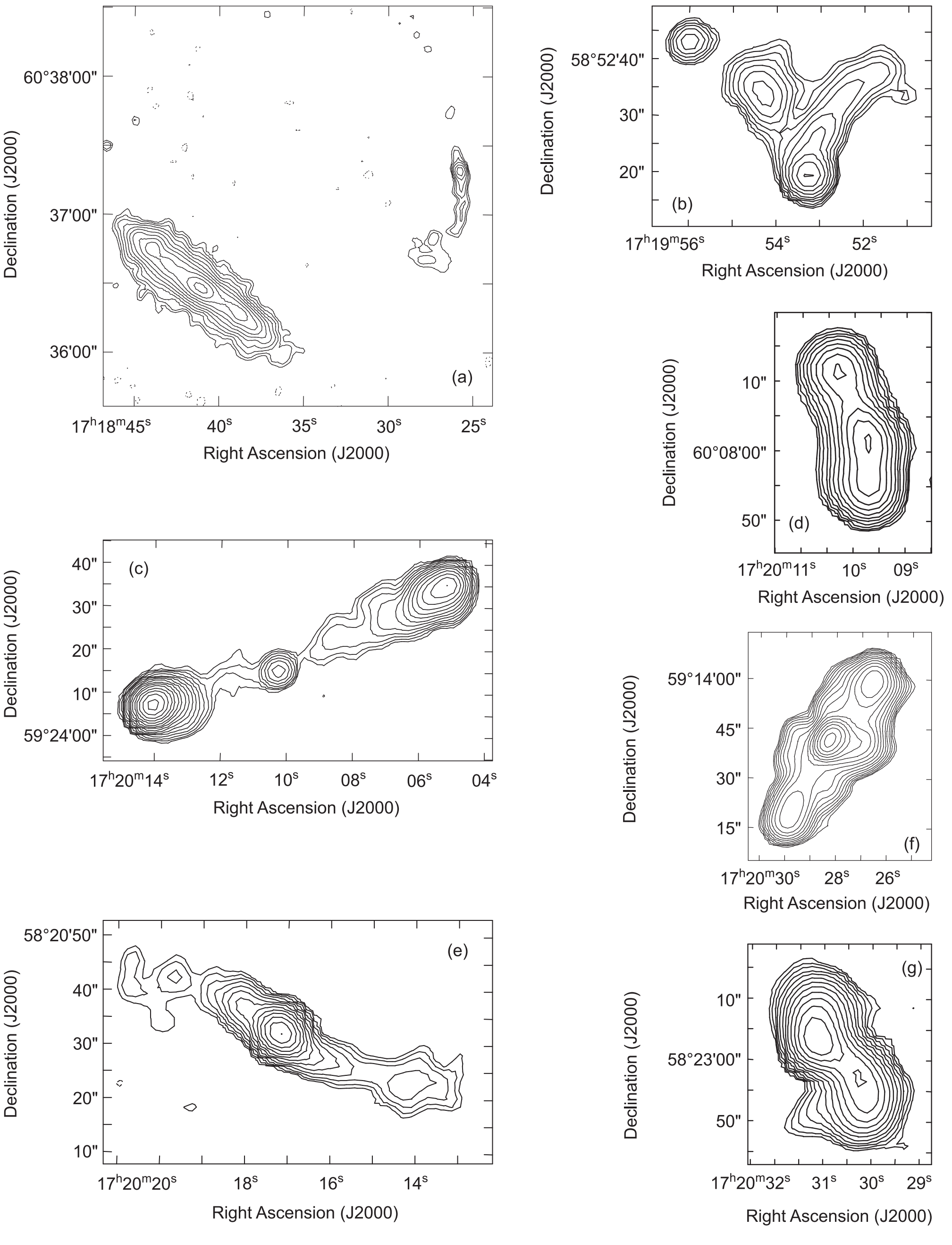

Fig. 10.— Complex sources. Contours are plotted at $\pm 50\,\mu\mathrm{Jy\ beam}^{-1} \times 2^{1/2}, 2^{1}, 2^{3/2}, 2^{2}, \ldots$

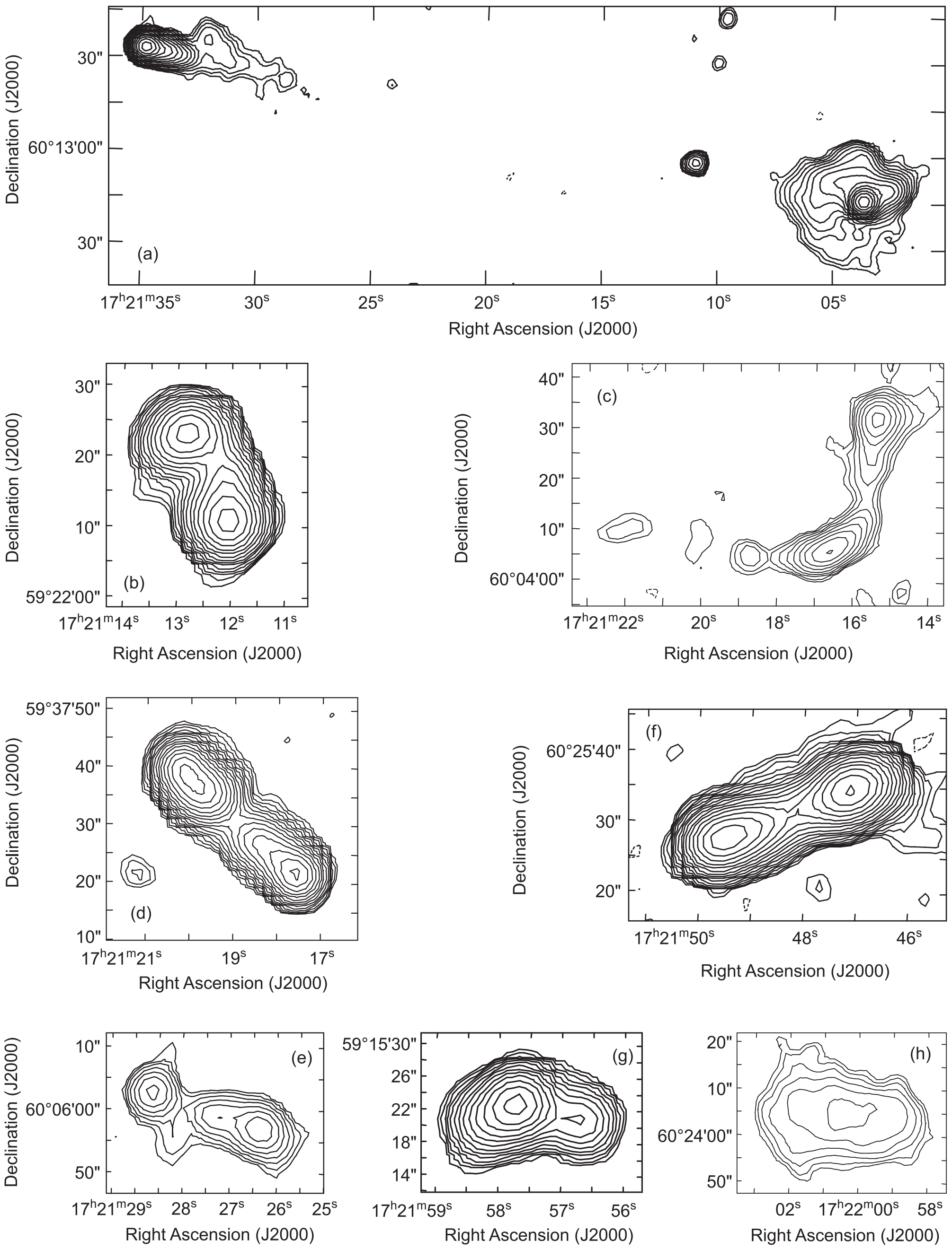

Fig. 11.— Complex sources. Contours are plotted at $\pm 50\,\mu\text{Jy beam}^{-1} \times 2^{1/2}, 2^{1}, 2^{3/2}, 2^{2}, \ldots$

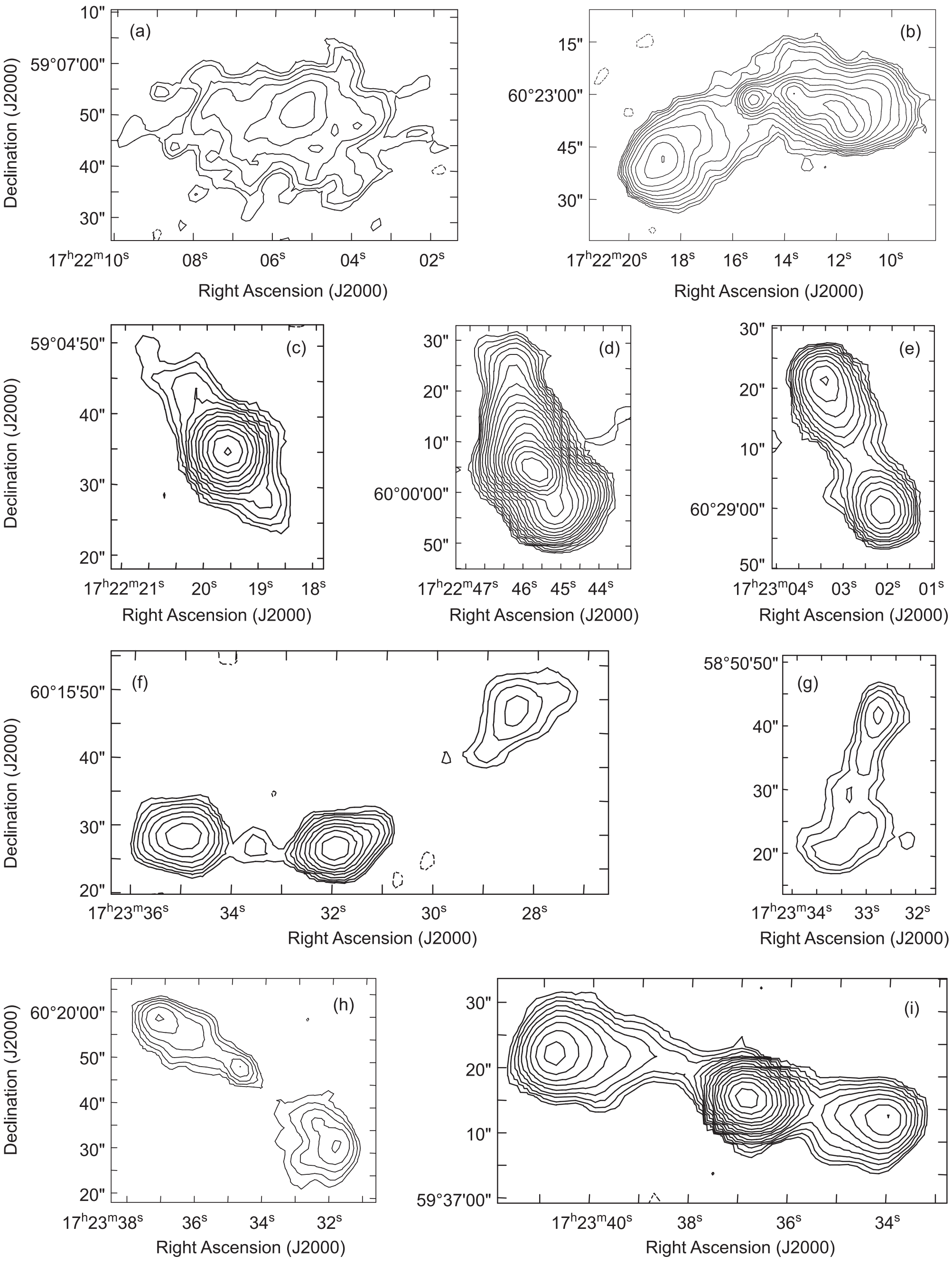

Fig. 12.— Complex sources. Contours are plotted at $\pm 50\,\mu$Jy beam$^{-1} \times 2^{1/2}, 2^{1}, 2^{3/2}, 2^{2}, \ldots$

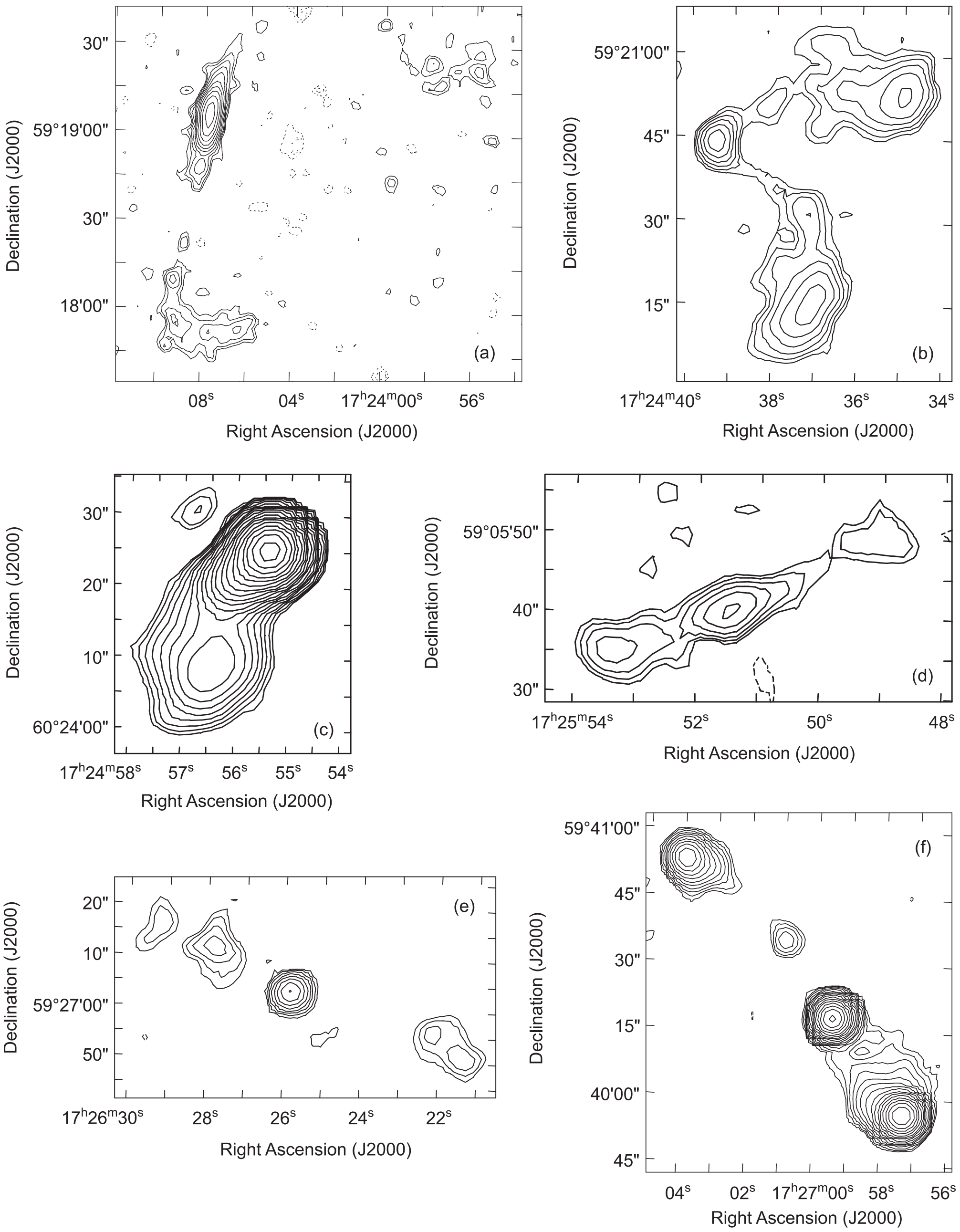

Fig. 13.— Complex sources. Contours are plotted at $\pm 50\,\mu$Jy beam$^{-1} \times 2^{1/2}, 2^1, 2^{3/2}, 2^2, \ldots$